Energy Storage Materials 67 (2024) 103324

Contents lists available at ScienceDirect

Energy Storage Materials

journal homepage: www.elsevier.com/locate/ensm

Strain-modulated Mn-rich layered oxide enables highly stable potassium-ion batteries

Hong Wang [a,b,c], Jiashen Meng [a], Zhitong Xiao [a], Wen Liu [a], Fang Liu [a,c], Yan Li [a], Liang Zhou [a,*], Jinsong Wu [a,c,*]

[a] State Key Laboratory of Advanced Technology for Materials Synthesis and Processing, School of Materials Science and Engineering, Wuhan University of Technology, Wuhan 430070, China
[b] School of Mathematics and Physics, Jingchu University of Technology, Jingmen 448000, China
[c] Nanostructure Research Center (NRC), Wuhan University of Technology, Wuhan 430070, China

ARTICLE INFO

Keywords:
Strain-modulated
Mn-rich layered oxide
Potassium ion batteries
Jahn-Teller distortion
Internal strain

ABSTRACT

Mn-rich layered oxides show great promise as cathode materials for potassium-ion batteries due to their high capacity and cost-effectiveness. However, internal structural strain and irreversible phase transitions caused by Jahn-Teller distortion affect their cycling stability. Here, we present an efficient strategy to concurrently modulate the internal strain and suppress the irreversible phase transition in Mn-rich cathodes by incorporating amounts of zinc (Zn) ions into the transition metal layers. The substituted Zn serves to regulate local chemistry, thereby mitigating octahedral distortion in Mn-O bonds, relieving the strain between layers, and reducing the occurrence of P3-O3 phase transition under high voltages. These findings are supported by EXAFS, in situ X-ray diffraction, advanced transmission electron microscopy, electron tomography, and DFT simulations. The low-strain $K_{0.5}Mn_{0.8}Co_{0.1}Zn_{0.1}O_2$ electrode exhibits a high reversible capacity retention about ~90 % (105 mAh g^{-1} at 100 mA g^{-1}), exceptional rate performance in the voltage of 1.5 ~ 3.9 V, and a substantial capacity retention after 500 cycles. This strain-relieved approach broadens the scope of lattice engineering by addressing internal strain concerns and mitigating the strain associated with potassium (de)intercalation, thereby having potential to advance the development of stable cathodes for PIBs.

1. Introduction

Due to the rising cost of lithium resources, potassium ion batteries (PIBs), benefited from high content potassium in earth's crust and cheap price, are considered as one of the promising alternatives [1–5]. Various cathode materials have been investigated as key determinants for PIBs, including transitional oxides [6–7], polyanionic compounds [8] and alkali-metal hexacyanometalates [9]. Among these materials, potassium-based layered transition-metal oxides (K_xTMO_2, TM=Mn, Co, Ni, *etc.*) have gained significant attention due to their high theoretical capacities, low cost and environmental friendliness [10–12]. However, despite their immense potential, these oxides electrodes often suffer from capacity decay during extended electrochemical cycles [13]. The valence of Mn in Mn-based layered oxides usually stays between 3+ and 4+. Induced by Mn^{3+} ions ($t_{2g}^3e_g^1$), these materials tend to undergo large Jahn-Teller distortions during K^+ insertion/retraction, leading to severe cyclic degradations [14,15]. As a typical element with Jahn-Teller effect, high spin Mn^{3+} ($t_{2g}^3e_g^1$) causes an abnormal bond length change of O-Mn-O in [MnO_6] octahedral [5,16]. Therefore, inhibiting severe Jahn-Teller distortion caused by massive $Mn^{3+}$to improve its cycling stability are of great importance.

In the research of Li- and Na-ion batteries, considerable efforts have been dedicated to mitigating structural degradation caused by Jahn-Teller distortions through various strategies, such as structure engineering, elemental doping, and coating [17–19]. Yu *et al.* designed linearly decreased Mn and increased Ni and Co from center to the surface of agglomerated-sphere LLOs and the cathode exhibited enhanced electrochemical performance [20]. Indranil *et al.* reported successful Ti^{4+} doping as a means of substituting Mn and Fe atoms in P2 $Na_{0.67}Fe_{0.5}Mn_{0.5}O_2$, and the Ti^{4+} doping led to an increased Na-layer spacing and demonstrated improved structural stability [21]. These strategies are achieved by increasing the Mn valence in the pristine state (*i.e.*, the state present in the original, unaltered sample prior to cycling). Increasing Mn valence state to 4+ can reduce octahedron spin caused by

* Corresponding authors.
E-mail addresses: liangzhou@whut.edu.cn (L. Zhou), wujs@whut.edu.cn (J. Wu).

https://doi.org/10.1016/j.ensm.2024.103324
Received 10 January 2024; Received in revised form 26 February 2024; Accepted 4 March 2024
Available online 5 March 2024

Mn^{3+}, restrain the anisotropic Mn-O bond lengths, thus improve its structural stability [22,23]. However, during the cycling process, the Mn^{3+}/Mn^{4+} redox couple serves as the primary mechanism for charge compensation. This results in the repeated formation of Mn^{3+} and Mn^{4+}, which in turn induces recurring Jahn-Teller distortions and the restoration of the MnO_6 octahedrons. Thus, mitigating these dynamic Jahn-Teller distortions and their corresponding electromechanical stress becomes crucial in order to minimize volume changes during cycling, thus enhancing the overall stability of the cycling process. Furthermore, it is important to note that achieving an oxidized Mn^{4+} state in the pristine state does not guarantee a crystal structure with zero strain. Even in the pristine state, complex lattice strain can originate from other sources and contribute to the overall strain [24].

The anisotropic lattice strain can have two origins: electromechanical strain, occurring when K^+ shuttles back and forth, and intrinsic strain stemming from the crystal structure itself [25]. Electromechanical strain primarily originates from the variation of ionic radius of redox species and oxygen repulsions in high voltages, contributing to the contraction of transition metal-oxygen octahedrons (TMO_6) and electrostatic interaction (O-O and O-K-O) [26]. During the K^+ insertion/-retraction, the valence of Mn fluctuates between 3+ and 4+, resulting in repeatedly removed and restored Jahn-Teller distortion [27]. The distortion may also lead to inhomogeneous strain, resulting rapid structural evolution and penetrative cracking [28]. The intrinsic strain in layered oxides are rarely investigated. Previously studies show the tilting of TMO_6 octahedral may induce shear strains in perovskites, which influences the Jahn-Teller distortion [29]. The Mn-O axial bonds in a non-linear molecular system (MnO_6) may experience geometric distortion, resulting in two longer and two shorter bonds (as opposed to the equatorial Mn-O bonds in undistorted structures). This distortion typically reduces crystalline symmetry, causing structural disorder and significant intrinsic strain, leading to a pseudo Jahn-Teller effect [30]. Wei *et al.* found inhomogeneous interlaminar stress originated from the intrinsic structural transitions creates surface cracks in $Na_{0.65}Mn_{0.67}Co_{0.17}Ni_{0.17}B_{0.05}O_{2+y,}$ and they constructed a spinel-like/layered heterostructure to prevent the accumulation of stress and lattice distortion [31]. Wang *et al.* observed surficial oxygen loss and phase transition in $K_{0.5}Mn_{0.8}Co_{0.2}O_2$ layered oxide and constructed a thin $K_3PO_4/MnPO_4$ layer to protect lattice expansion and contraction in cycling [32]. Nevertheless, these strategies merely address surface issues, leaving the underlying problem of internal stress unresolved [33,34]. The occurrence of anisotropic lattice strain due to dynamic Jahn-Teller distortion, along with the intrinsic strain, can lead to structural degradation, penetrative cracking and capacity decay in cycling.

In this work, in order to alleviate lattice strain induced by the dynamic Jahn-Teller distortion, we introduce zinc ions into the potassium layered transition-metal oxide $K_{0.5}Mn_{0.8}Co_{0.2}O_2$ (KMCO). Zn substitutes the transitional metal elements, Mn and Co, as studied by atomic resolution HAADF-STEM image and EDS mapping. The presence of Zn^{2+} has reduced the interlayer spacing of the (003) lattice plane, reducing the tilting of TMO_6 octahedrons and the intrinsic shear strain that arises from symmetry breaking in the layers. Furthermore, the successful incorporation of zinc into the Mn/Co layer stabilizes the energy of the Mn-O bonds and eliminates the degeneracy of the electron configuration. This, in turn, weakens the dynamic Jahn-Teller distortion and effectively suppresses the phase transition from P3 to O3 that can occur under high voltage conditions. Thus, the $K_{0.5}Mn_{0.8}Co_{0.1}Zn_{0.1}O_2$ (KMCZO) electrode delivered a reversible charge/discharge capacity of 105 mAh g^{-1} with a capacity retention of 89.8% even after 100 cycles at 100 mA g^{-1}. The results offer a potential solution to alleviate intrinsic strain and enhance the structural stability of Mn-based layered oxide cathode materials.

2. Results and discussions

2.1. Structural analyses of the pristine KMCO and Zn^{2+}substituted KMCZO

$K_{0.5}Mn_{0.8}Co_{0.2}O_2$ (KMCO) was synthesized via a sol-gel method, with subsequent heating treatment at 800 °C for 10 h, as detailed in the supporting information, while $K_{0.5}Mn_{0.8}Co_{0.1}Zn_{0.1}O_2$ (KMCZO) was synthesized by adding $Zn(NO_3)_2{\cdot}6H_2O$ in the appropriate molar mass proportion. Inductive coupled plasma emission spectrometer (ICP) are carried out to determine the proportion of elements of the two samples and results are listed in Table S1, showing the K, Mn and Co ratios match to the theoretical chemical formulas. The scanning electron microscope (SEM) images (Fig. S1) show analogous morphology of KMCO and KMCZO, illustrating that the introduction of Zn^{2+} does not influence the appearance of the synthesized nanoparticles.

A series of $K_{0.5}Mn_{0.8}Co_{0.2-x}Zn_xO_2$ (x = 0, 0.05, 0.1, 0.2) layered oxides, abbreviated as KMCO, KMCZO-0.05, KMCZO-0.1, KMCZO-0.2, respectively, were synthesized by the sol-gel method. The structure of the synthesized samples was studied by XRD, as shown in Fig. S2. The pristine KMCO presents a typical P3 structure with a hexagonal lattice and space group of *R*3*m*. With the increase of Zn content, the structure can be well maintained as the P3 structure. When the substitution content is smaller than 0.2, the layered spacing {00l} keeps decreasing with the increased Zn content, implying a reduction in the TM-O bond. Thus, the stretching of Mn-O bonds has been alleviated, leading to a mitigation of the shear strain on MnO_6 octahedrons. However, when the Zn content continues to increase (say when it is 0.2), Zn^{2+} start to occupy K^+ sites. This may lead to a severe Jahn-Teller distortion and internal layer strain. Thus, KMCZO-0.1 is identified as the sample with the most appropriate Zn content.

In order to investigate the crystalline structures and uncover any internal strain fatigue or Jahn-Teller distortion in KMCO and KMCZO, we utilized X-ray diffraction (XRD), X-ray photoelectron spectroscopy (XPS), and X-ray absorption near-edge structure (XANES), as illustrated in Fig. 1 and Fig. S3. To determine crystalline structure of both samples, Rietveld refinements are conducted, as shown in Fig. 1a-c. Both KMCO and KMCZO have a P3-type layered structure with a hexagonal lattice and space group of *R*3*m*. The TM^{n+} elements (where TM=Mn, Co or Zn) occupy octahedral sites, while K^+ occupy the prismatic sites. Moreover, the parallel layers containing O ions are arranged in an ABBCCA sequence. The detail refinement results and structural information of the two structures are listed in Table S2-S3. The increase of the lattice parameter *a* is mainly due to the increase of TM-to-TM length. As there is difference in ionic radius between Co^{3+}(63 pm) and Zn^{2+}(74 pm), the substitution of Zn enlarges the lattice parameter *a*.

Three salient characters of KMCZO different from KMCO can be figured out. Firstly, it is noted that the (003) peak in KMCZO has exhibited a shift towards a higher angle, as compared to that observed in KMCO (Fig. 1a). This indicates that the (003) spacing has decreased due to Zn substitution, suggesting a reduction in the interlayer distance. Thus, the stretching of Mn-O bonds has been alleviated, leading to a mitigation of the shear strain on MnO_6 octahedrons. With Zn^{2+} occupying into TM layers, the spacing between TM layers is decreased. This leads to noticeable shrinkage of Mn-O bond lengths in the O-Mn-O direction. This reduces the uneven changes in Mn-O bond lengths in [MnO_6] octahedrons, thus lessens Jahn-Teller distortion. Moreover, the strong oscillation shown in EXAFS (Fig. 1g) shifts towards higher k, indicating the change in coordination bond length of Mn. Contour plots of Mn K-edge wavelet-transformed EXAFS spectra are shown in Fig. 1h-i. Peaks corresponding to Mn-O and Mn-M (M = K, Mn, Co, and Zn) coordination shells can be observed at approximately (5.0 $Å^{-1}$, 1.4 Å) and (6.5 $Å^{-1}$, 2.4 Å), respectively. In the case of KMCZO, the Mn-M feature appears elongated, while the intensity of the Mn-O feature is weakened compared to that in KMCO. This suggests that the environment of Mn ions has been altered due to Zn^{2+} substitutions, thus alleviating the

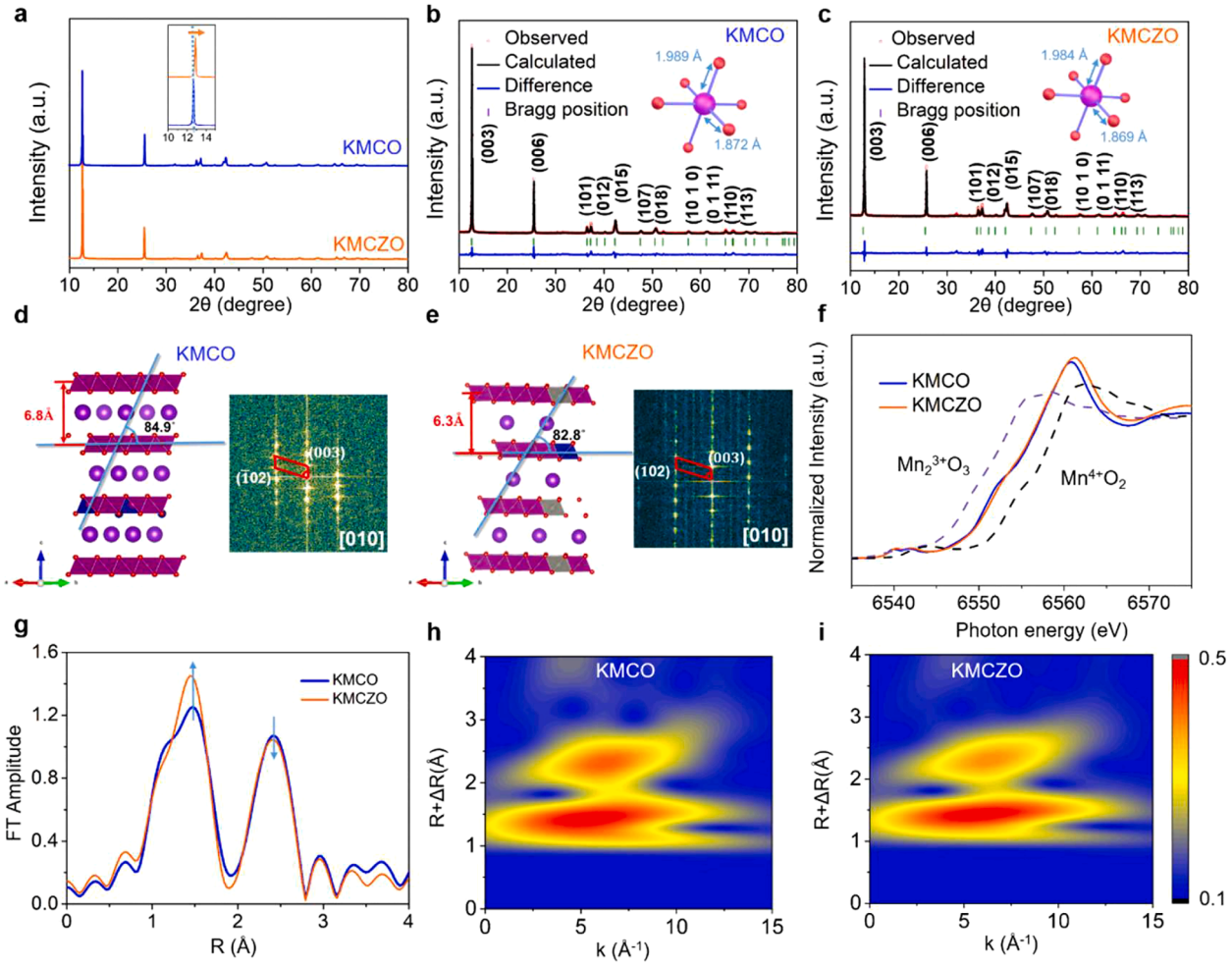

Fig. 1. Structural analysis of KMCO and KMCZO. (a) XRD pattern. (b, c) Rietveld plots of KMCO and KMCZO. (d, e) Illustration structures and corresponding FFT patterns. (f) Normalized K-edge XANES spectra of Mn. (g) Fourier transform of extended X-ray absorption fine structure (EXAFS) data of Mn. (h, i) Wavelet transforms of Mn K-edge in KMCO and KMCZO, respectively.

Jahn-Teller effect. Secondly, the atomic structures shown in Fig. 1d-e reveal the changes before and after Zn introduction. The angle between the (003) and (101) plane has decreased with the substitution of Zn (as measured from the FFT patterns), indicating the tilting of MnO_6 octahedrons in KMCZO has been alleviated. This will also lead to a mitigation of the shear strain of the interlayered MnO_6 octahedrons.

Thirdly, there is an increase in the Mn oxidation state induced by Zn^{2+} substitution, *i.e.* the averaged Mn valence in KMCZO is 3.608 compared to 3.539 in KMCO. To accurately determine the valence of Mn, XPS and XANES techniques were employed (Fig. 1f-i). The XPS survey of KMCO and KMCZO is depicted in Fig. S2a. The electronic structure of Mn in KMCO and KMCZO is revealed through the XPS spectra of Mn 2p, as shown in Fig. S2b-c. Due to the low content of Co in KMCZO, the Co peak intensity is relatively weak. By comparing these spectra with reference spectra of Mn_2O_3 and MnO_2 (Fig. 1f), it can be inferred that the average oxidation state of Mn in KMCO and KMCZO lies between Mn^{3+} and Mn^{4+}. However, the photon energy of Mn K-edge in KMCZO indicates a higher energy shift, implying an increase in the oxidation state of Mn following the substitution of Zn^{2+}. In Fig. S3d, the presence of a Zn signal in KMCZO confirms the successful incorporation of Zn. The results confirm that a portion of Mn^{3+} ions have been oxidized to the Jahn-Teller inactive Mn^{4+}, facilitated by Zn^{2+} substitution. Moreover, the Co valence in KMCZO is also increased compared to that in KMCO (Fig. S2e-f).

The pristine KMCO and Zn^{2+} substituted KMCZO are also characterized by aberration-corrected scanning transmission electron microscopy (STEM) at atomic resolution. High angle annular dark field (HAADF) STEM images of KMCO and KMCZO along the [010] zone axis is shown in Fig. 2a and 2c, respectively. The measured (003) d-spacing of KMCO is 0.68 nm (Fig. 2e), while that of KMCZO decreases to 0.63 nm (Fig. 2f), agree with the XRD results. The MnO_6 octahedra with little distortion is formed for Mn^{4+} and produces a stable crystal structure. However, the Jahn-Teller effect caused by Mn^{3+} induces geometric distortion in [MnO_6] octahedrons, resulting in two shorter or longer Mn-O axial bonds (Fig. 2g). From atomic-resolution EDS mapping (Fig. 2h-m), we can find that Mn, Co and Zn ions occupy the TM-metal ions' layers, while K^+ located between TM layers. This confirms that Zn^{2+} are located in transitional sites, replacing TM sites (a structural model is shown in Fig. 2f as an insert). It is interesting to note that the strain distribution in KMCZO is quite different from that of KMCO. By geometric phase analysis (GPA) analysis, a more fluctuated strain is found in KMCO (Fig. 2b), while the strain distribution in KMCZO is relatively more flat (Fig. 2d). This confirms that Zn substitution effectively alleviates variation of the internal strain in the pristine samples.

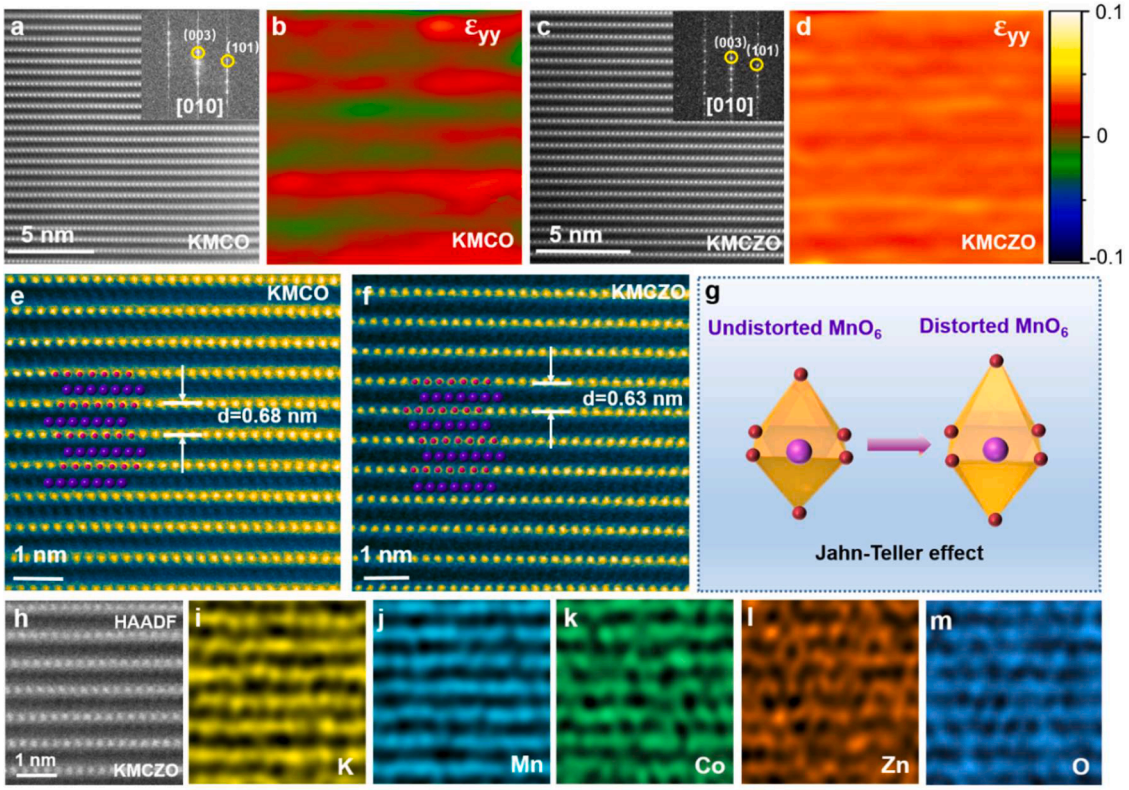

Fig. 2. Structural analysis of KMCO and KMCZO samples. (a) STEM image of KMCO. (b) Corresponding strain distribution of KMCO. (c) STEM image of KMCZO. (d) Corresponding strain distribution of KMCZO. (e) (f) STEM images of KMCO and KMCZO along [010] axis. (g) Diagram of Jahn-Teller distortion. (h)-(m) HAADF and the corresponding STEM-EDS mapping for K, Mn, Co, Zn and O, respectively.

2.2. Electrochemical performance of KMCO and KMCZO

The electrochemical performance of KMCO and KMCZO is compared to investigate the effect of Zn substitution. The cyclic voltammetry (CV) curves of KMCO and KMCZO were tested in half-cell PIBs from 1.5 V to 3.9 V (vs. K^+/K), respectively (Fig. S4a-b). Four pairs of redox peaks are observed in KMCO at 2.25/1.87, 2.45/2.30, 3.37/2.75 and 3.83/3.58 V. The redox peaks at 2.25/1.87 and 2.45/2.30 V are typically attributed to the Mn^{3+}/Mn^{4+} redox reaction, while the other two pairs at 3.37/2.75 and 3.83/3.58 V are associated with Co^{2+}/Co^{3+} redox and possibly also a portion of Mn-ion redox in higher charge state [32]. The four pairs of redox peaks are also observed in KMCZO. However, it is interesting to note that the redox couples at 2.28/2.04 and 2.65/2.47 V are strengthened while the peaks at 3.25/3.0 and 3.85/3.75 V are apparently weakened in KMCZO. Galvanostatic intermittent titration technique (GITT) test is performed at the first discharge cycle to investigate K^+ diffusion coefficient (Dk). The higher Dk values and lower overpotentials of KMCZO, as shown in Fig. S5 and Fig. 3a, compared to KMCO when discharged from 3.9 V to 1.5 V, indicate a swifter K^+ diffusion kinetics in KMCZO. The charge/discharge curves in Fig. 3b-c of KMCZO show a slope in the high voltage range compared to those in KMCO. After continuous K^+ insertion/retraction, the fading of redox reactions on the high voltage region is the main reason for the decrease in the capacity of KMCO materials. For example, the voltage platforms above 3.5 V in KMCO have gradually disappeared. In contrast, KMCZO cathodes have retained these voltage platforms to some extent. In Fig. 3d, the cycling stability demonstrates that KMCZO achieved a high reversible discharge capacity of 105 mAh g^{-1} with a capacity retention of 89.8 % after 100 cycles at 100 mA g^{-1}. In contrast, KMCO only exhibited a discharge capacity of 75.4 mAh g^{-1} with 70.1 % capacity retention. These findings indicate that Zn substitution stabilizes the redox reaction in the high voltage region. KMCZO also has a better rate performance as it shows a higher discharge capacity of 117, 108, 105, 99 and 84 mAh g^{-1} at 100, 200, 300, 500, 1000 and 2000 mA g^{-1}, compared to 112, 100, 92, 82, 70 and 62 mAh g^{-1} obtained by KMCO (Fig. 3e). Low polarization of KMCZO is indicated by the charge/discharge curves of rate capability (Fig. 3f and Fig. S6). For long cycling performance in Fig. 3g, KMCZO has achieved a higher reversible capacity retention of ~72.2 %, while KMCO stayed ~42.8 % after 500 cycles at 1 A g^{-1}. The corresponding differential capacity traces (dQ/dV) in Fig. S7 provide in-depth information. KMCZO has a larger reversible capacity and a better reversibility of Mn redox process at lower potential, compared to KMCO. The resistances fitted by EIS results are also conducted in Fig. S8. Long-term cycling stability beyond 500 cycles shows that KMCZO has a capacity retention of 57.7 % even after 800 cycles at 1 A g^{-1} (Fig. S9). The electrochemical impedance spectroscopy (EIS) plots reveal that KMCZO exhibits a significantly lower Rct value compared to KMCO, indicating enhanced ion transport mobility. This is supported by the EIS results, GITT data, and long cycling performance, which demonstrate that the intrinsic strain between the layers has been alleviated after Zn^{2+} occupying TM site, and the Mn^{3+} distortion from the dynamic Jahn-Teller effect has been alleviated, thereby improving its electrochemical performance. Compared with previously reported layered cathodes in PIBs (Fig. 3h), KMCZO exhibits a competitive K^+ storage in both capacity and cycling stabilities. The presence of Zn^{2+} has reduced the interlayer spacing of the (003) lattice plane, reducing the tilting of TMO_6 octahedrons and the intrinsic shear strain that arises from symmetry breaking in the layers. This creates an environment to have more active K-ions participating into the charge/discharge cycles. The successful incorporation of zinc into the Mn/Co layer stabilizes the energy of the Mn-O bonds and eliminates the degeneracy of the electron configuration. This, in turn, weakens the dynamic Jahn-Teller distortion and effectively suppresses the phase transition from P3 to O3 that can occur under high voltage conditions. Mitigating the strain and thus

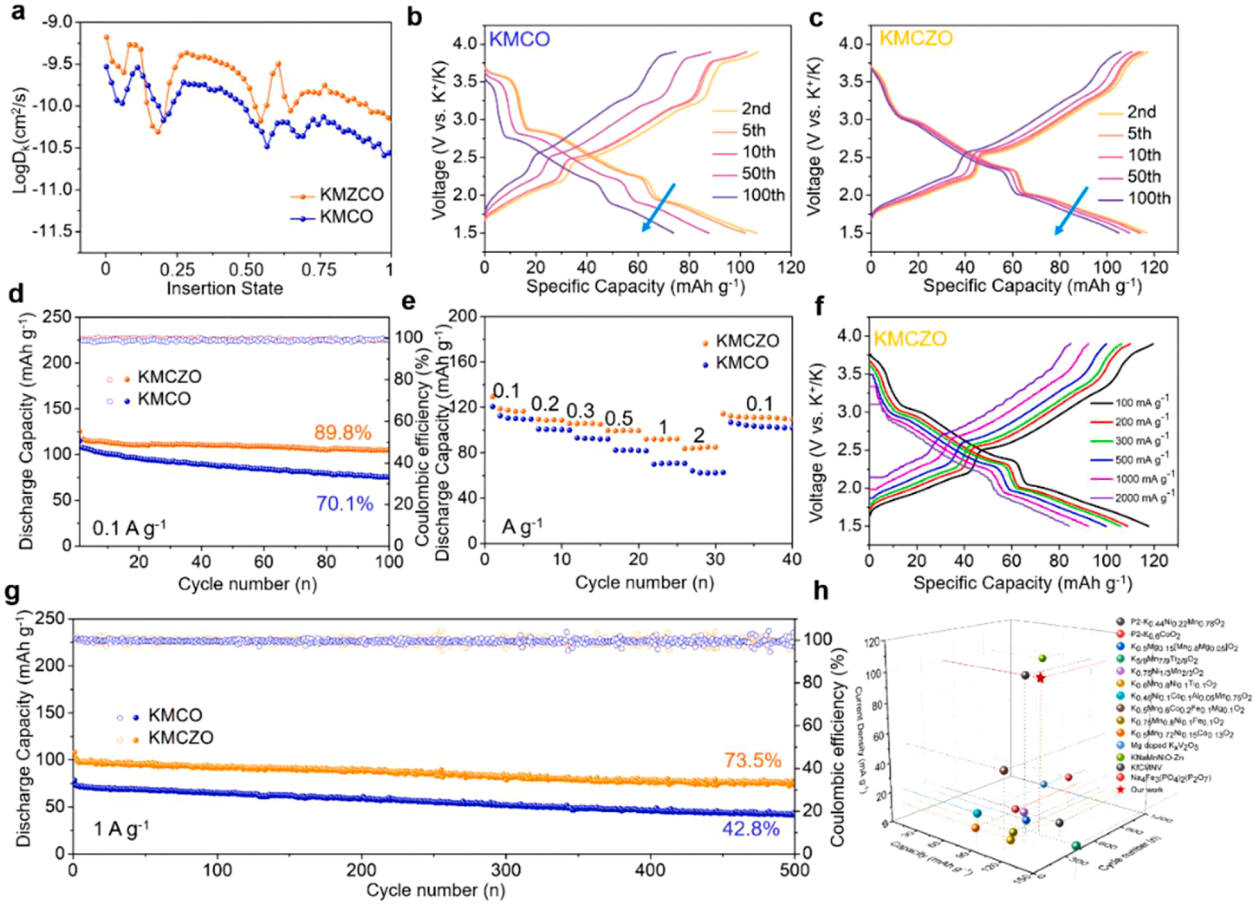

Fig. 3. Electrochemical properties of KMCO and KMCZO. (a) K^+ diffusion coefficients of KMCO and KMCZO from GITT tests. (b, c) Charge and discharge voltage profiles of KMCO and KMCZO at 0.1 A g^{-1}. (d) Cycling performance at 0.1 A g^{-1}. (e) Rate performance of KMCO and KMCZO at various current densities from 0.1 A g^{-1} to 2 A g^{-1}. (f) Charge and discharge voltage profiles of KMCZO at various current densities. (g) Long term cycling performance of KMCO and KMCZO at 1 A g^{-1}. (h) Comparison of capacity, cycle number and current density for KMCZO with previously reported potassium cathodes.

volumetric changes in charge/discharge has thus created more active sites for K-ion insertion and extraction.

A schematic illustration of the assembled KMCZO||K@CC pouch cells is shown in Fig. S10. The pouch cell exhibits a discharge capacity of approximately 115 mAh g^{-1}, and a capacity retention of 74.2 % at 0.1 A g^{-1}. Two pouch cells connected in series are used to power 50 three-color light emitting diodes (LEDs). This demonstrates the stable cyclability and relatively low voltage decay of the pouch cell, highlighting the advantages of Zn^{2+} substitution in alleviating lattice strain and dynamic Jahn-Teller distortion.

2.3. *Mitigated dynamic Jahn-Teller distortion in cycling due to Zn substitution*

During K^+ insertion/retraction, the structural evolution of KMCO and KMCZO is monitored by in situ XRD in the voltage window of 1.5–3.9 V. As illustrated in Fig. 4a, the P3 phase is maintained up to 3.2 V during the initial charge. Simultaneously, the value of *c* increases, as evidenced by the shift of the (006) peak to a lower angle. This increase is attributed to the repulsive force between the adjacent oxygen layers during K^+ extraction. Additionally, there is a slight contraction of the *a-b* plane, indicated by the shift of the (012) peak to a higher angle. This contraction is caused by the smaller ion radius of Mn at the valence state of 4^+. When the voltage is higher than 3.2 V upon further K^+ extraction, the (012) and (015) peaks of P3 phase disappear. Meanwhile, the appearance of the O3 (104) peak at ~41.7° confirms the occurrence of the P3 to O3 phase transition. In the following discharge, the O3 phase reversibly transforms back to P3 phase, as the (012) and (105) peaks of P3 phase reappear. The P3 (006), (101), (012) and (015) peaks can also reversibly shift back upon further discharging. Therefore, KMCO undergoes a phase transition between P3 and O3 phase at high voltage, triggered by TMO_6 gliding and promoted by the dynamic Jahn-Teller distortion. The large structural reorganization during phase transition will usually lead to rapid capacity fading and quick structural degradation.

KMCZO undergoes a similar shift of the P3 peaks and the phase transition at high voltage (Fig. 4b). However, the voltage region within which P3 and O3 phase transition occurs has been obviously shortened, say from 3.2 V to 3.9 V in charge process and 3.9 V to 2.7 V in discharge process. In KMCO, the strong O3 (104) peak appeared, while the P2 (006) peak has also been greatly weakened, showing a nearly completed P2-to-O3 phase transition (Fig. 4c). However, the P2-to-O3 phase transition is only partially accomplished in KMCZO. Although the O3 (104) peak is also observed, the intensity of the leak is weak, and the intensity of the P2 (006) peak stay almost unchanged (Fig. 4d-f). Meanwhile, the lattice shear strain between the TM layers and Jahn-Teller effect are weakened during charge and discharge, as evidenced by the smaller P2 (006) peak shift (0.89°) in KMCZO, which is smaller than that of KMCO (1.06°) in the first two K^+ insertion/retraction process. Moreover, the changes of a parameter in KMCZO measured by shift of the (012) peak are also smaller than those in KMCO (Fig. S11). Thus, the Zn-substituted Mn-based layered oxide mitigate the dynamic Jahn-Teller distortion, which effectively suppress the destructive phase transition.

The microstructures of the cycled KMCO and KMCZO (*e.g.* after 50

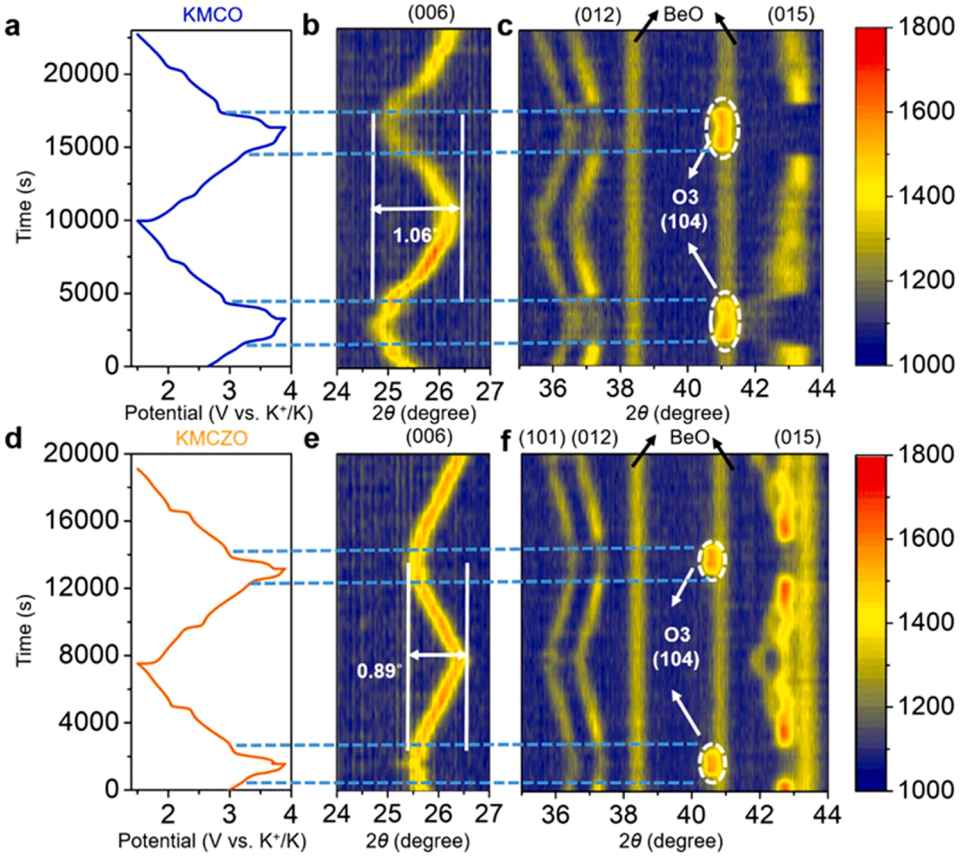

Fig. 4. *In situ* XRD characterization of KMCO and KMCZO. (a) Charge and discharge curves of KMCO. (b, c) Corresponding peaks' changes during the first and second cycle in KMCO. (d) Charge and discharge curves of KMCZO. (e, f) Corresponding peaks' changes during the first and second cycle in KMCZO.

cycles) have also been studied by STEM imaging and three-dimensional (3D) electron tomography. Severe nanoscale cracks and lattice distortion on the surface are observed in KMCO (Fis. S12 a-b and S13). Spinel structure is also observed on the surface of KMCO, indicating the phase transition occurred during repeated K^+ insertion/retraction. The reconstructed volume of the KMCO particle cycled by 50 cycles clearly demonstrates the nano cracks on the surface (Fig. 5a). For a better view, the rotation, filtering and orthoslicing process of the reconstructed KMCO are presented in temperature color mode in Video S1. However, in cycled KMCZO (Fig. S12 c-d), only slightly lattice distortion is observed. KMCZO exhibits fewer surface cracks than KMCO. HAADF-STEM image and EDS mapping of the cycled KMCZO (Fig. S12 e-j) and 3D tomography reconstruction (Fig. 5b and Video S2) confirm that the overall structure is well maintained, implying the Zn^{2+} substitution can effectively alleviate the lattice strain and suppress Jahn-Teller effect.

After 100 cycles, the strong oscillation illustrated in EXAFS shifts towards higher k in KMCZO, indicating the more reversible coordination bond length of Mn in KMCZO than in KMCO (Fig. S14). The intensity of the Mn-M (6.5 $Å^{-1}$, 2.4 Å) is increased compared to pristine samples, indicating the environment of Mn ions has been altered in both samples. These results show that Zn substitution leads to a better structural stability after cycling. Ex situ XPS was conducted to study charge

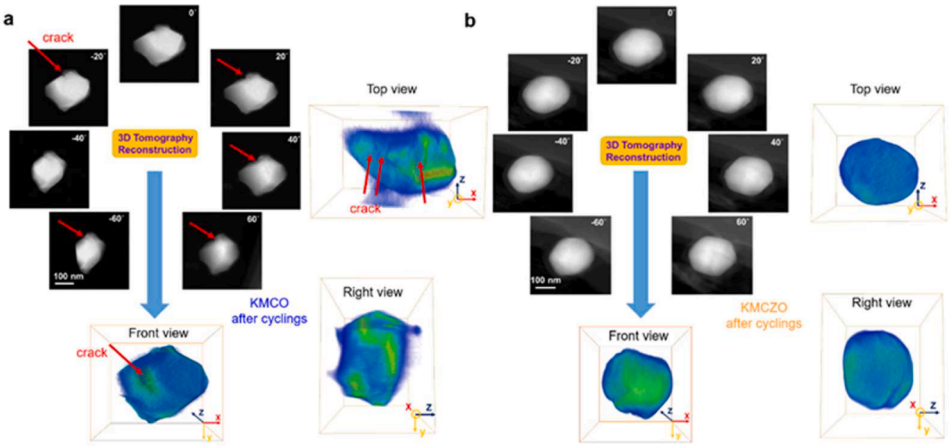

Fig. 5. Synchrotron-based TXM tomography. (a) (b) Representative STEM-HAADF images of individual KMCO and KMCZO particles after 50 cycles at 0.1 A g^{-1} at different rotation angles and reconstructed KMCO and KMCZO particles from front, top and right views, respectively.

compensation in the cycled KMCO and KMCZO across various states. As has shown in Fig. S15, Mn-ions' charge state in KMCO undergo a process of first increasing and then decreasing. In KMCZO, Mn-ions' charge state has gone through a similar process except that in the 3.9 V charged state, Mn^{3+} have completely disappeared. In Fig. S16, different charged and discharged states of Zn are illustrated. The Zn 2p peak did not shifted at different electrochemical process, indicating that Zn did not participant in the redox process. These phenomena prove that Mn^{3+}/Mn^{4+} redox process in KMCZO during charge and discharge are more reversible than that in KMCO.

2.4. DFT calculations confirm strain relieved performance

Aiming to fully understand lattice strain and Jahn-Teller effect on Mn-based layered oxides, density functional theory (DFT) calculations are performed to investigate the influences of Zn^{2+} substitutions on crystal structure of both KMCO and KMCZO through bandgap and K^+ migration energy barriers. Fig. 6a and b present the schematic crystal structure of KMCO with the optimal migration path. In the case of KMCZO, Zn atoms partially replace TM atoms. The climbing image nudged elastic band method is utilized to calculate the K^+ migration barrier, yielding a value of ~0.77 eV for KMCO and ~0.65 eV for KMCZO (Fig. 6c). Consequently, the introduction promotes K^+ diffusion. Additionally, the total DOS in the vicinity of Fermi level is higher for KMCZO compared to KMCO, indicating an increased ion conductivity. This finding aligns with the EIS results. There are two types in Mn 3d electronic orbitals in MnO_6 octahedra: e_g (d_{z^2} and $d_{x^2-y^2}$) and t_{2g} (dxz, dyz, dxy). The t_{2g} orbitals in Mn^{4+} are fully occupied while the e_g orbitals are unoccupied, resulting in a homogeneous electronic cloud and equal lengths of the Mn^{4+}-O bonds. On the other hand, the Mn^{3+} orbitals exhibit a splitting effect near the Fermi level, with the unoccupied $d_{x^2-y^2}$ orbital and the occupied d_{z^2} orbital. This splitting is caused by the Jahn-Teller distortion, which elongates the Mn^{3+}-O bond and weakens the electrostatic repulsion between the electron clouds of the p_z orbital of O^{2-} in the octahedral corners and the d_z^2 orbital of Mn^{3+} in the octahedral center. Additionally, in KMCO, the high energy e_g orbitals split into two groups near the Fermi level. The splitting suggests the presence of Mn^{3+} which are active in generating Jahn-Teller distortion. Conversely, the e_g orbitals of Mn in KMCZO are not split, indicating Mn in this compound are Jahn-Teller inactive Mn^{4+} (Fig. 6d-e). The density of states (DOS) of KMCO and KMCZO are plotted in Fig. S17 to illustrate the electronic behavior. From the total DOS, the Zn dopant contributes largely to the total DOS of the system, including the states at −8, −0.2 and 4 eV. The superb reaction kinetics of the present material can be accounted for by examining the density of states (DOS) in KMCO and KMCZO for K-s orbitals, O-p orbitals, and transition-metal-d orbitals. These orbitals exhibit metallic properties, which contribute to the distinguished cycling stability of the material (Fig. S17a-b). Moreover, the charge density distribution of Mn-O in Fig. S17c-d reflects that the interaction between Mn and O is more intense after Zn substitution, demonstrating a more stable Mn-O bond in KMCZO. The fast electronic conductivity of the material is attributed to these metallic properties. Moreover, Zn^{2+} substitution in TM layers adjusts the proper K layer spacing and provides more K^+ diffusion channels. This minimizes the irreversible P3-O3 phase transition and maintains the structural stability during cycling. Additionally, the Zn orbitals are overlapped with the O 2p orbital close the Fermi level, leading to significant deformation of the electronic property of the KMCZO.

3. Conclusions

In summary, the introduction of Zn^{2+} into the TM layers of Mn-rich layered oxides has successfully alleviated internal structural strain and irreversible phase transitions caused by the Jahn-Teller effect. This modulation is achieved by adjusting the degree of Mn-O bond distortion within the lattice. The increased valence of Mn through Zn^{2+} incorporation regulates the local chemistry, reducing the octahedral distortion of Mn-O bonds and releasing the strain between the layers. Additionally, the occurrence of the P3-O3 phase transition under high voltages is mitigated. DFT calculations support these observations, attributing the enhanced phase stability and cycling performance to the suppressed lattice strain and Jahn-Teller effect resulting from Mn valence regulation. The elimination of lattice distortion and the prevention of intragranular crack nucleation, caused by inhomogeneous internal stress, lead to crack-free grains in the layered oxide materials. These crack-free grains ensure connectivity between the TM layers and superior electronic conductivity. The strain-modulated KMCZO electrode demonstrates a high reversible capacity of 105 mAh g^{-1} at 100 mA g^{-1} and a remarkable capacity retention of 72.2 % after 500 cycles. This work might offer fresh insights into cathode material design through structure engineering and provide a reference for the optimization of Mn-based layered oxides in PIBs.

CRediT authorship contribution statement

Hong Wang: Writing – original draft, Methodology, Investigation,

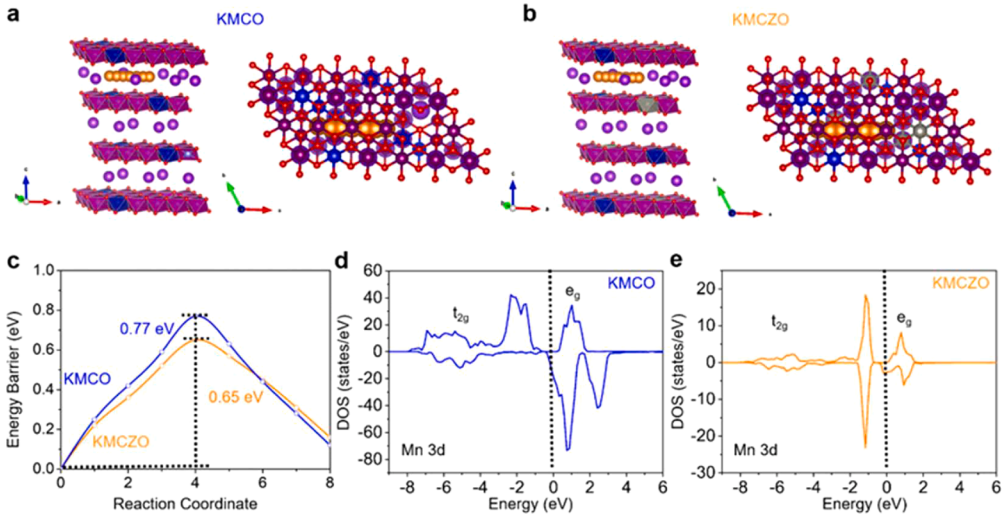

Fig. 6. Structural calculations. (a) K^+ migration pathway in KMCO. (b) K^+ migration pathway in KMCZO. (c) The corresponding migration energy profile in KMCO and KMCZO. (d) (e) Density of states of KMCO and KMCZO.

Formal analysis, Data curation, Conceptualization. **Jiashen Meng:** Writing – review & editing, Investigation, Data curation. **Zhitong Xiao:** Methodology, Investigation, Data curation. **Wen Liu:** Data curation. **Fang Liu:** Investigation. **Yan Li:** Software. **Liang Zhou:** Supervision, Project administration. **Jinsong Wu:** Writing – original draft, Supervision, Funding acquisition, Conceptualization.

Declaration of competing interest

The authors declare that they have no known competing financial interests or personal relationships that could have appeared to influence the work reported in this paper.

Data availability

Data will be made available on request.

Acknowledgements

This work was supported by the National Natural Science Foundation of China (52072282, 52150710537 and 52127816), the Scientific Research Foundation of Jingchu University of Technology (YB202214), the Key Research and Development Program of Hubei Province (2021BAA070) and the Shenzhen Fundamental Research Program (JCYJ20190809114409397).

Supplementary materials

Supplementary material associated with this article can be found, in the online version, at doi:10.1016/j.ensm.2024.103324.

References

[1] L. Wang, T. Liu, T. Wu, J. Lu, Strain-retardant Coherent Perovskite phase stabilized Ni-rich cathode, Nature 611 (2022) 61–67, https://doi.org/10.1038/s41586-022-05238-3.
[2] Z. Huang, Z. Gu, Y. Heng, E. Ang, H. Geng, X. Wu, Advanced layered oxide cathodes for sodium/potassium-ion batteries: development, challenges and prospects, Chem. Eng. J. 452 (2023) 139438, https://doi.org/10.1016/j.cej.2022.139438.
[3] J.B. Goodenough, Evolution of strategies for modern rechargeable batteries, Accounts Chem. Res. 46 (5) (2013) 1053–1061, https://doi.org/10.1021/ar2002705.
[4] X. Wang, Z. Xiao, K. Han, X. Zhang, Z. Liu, C. Yang, J. Meng, M. Li, M. Huang, X. Wei, L. Mai, Advances in fine structure optimizations of layered transition-metal oxide cathodes for potassium-ion batteries, Adv. Energy Mater. 13 (2) (2023) 2202861, https://doi.org/10.1002/aenm.202202861.
[5] X. Min, J. Xiao, M. Fang, W.A. Wang, Y. Zhao, Y. Liu, A.M. Abdelkader, K. Xi, R. V. Kumar, Z. Huang, Potassium-ion batteries: outlook on present and future technologies, Energ. Environ. Sci. 14 (4) (2021) 2186–2243, https://doi.org/10.1039/D0EE02917C.
[6] Y. Du, Z. Zhang, Y. Xu, J. Bao, X. Zhou, Metal sulfide-based potassium-ion battery anodes: storage mechanisms and synthesis strategies, Acta Phys.-Chim. Sin 38 (2022) 2205017, https://doi.org/10.3866/PKU.WHXB202205017.
[7] J. Liao, Q. Hu, X. Sheng, Z. Zhang, Y. Xu, X. Mo, X. Zhou, Corrugated layered titanates as high-voltage cathode materials for potassium-ion batteries, ACS Materials Lett. 4 (2022) 1653–1659, https://doi.org/10.1021/acsmaterialslett.2c00531.
[8] J. Hu, Y. Hong, M. Guo, Y. Hu, W. Tang, S. Xu, S. Jia, B. Wei, S. Liu, C. Fan, Emerging organic electrodes for Na-ion and K-ion batteries, Energy Storage Mater. 56 (2023) 267–299, https://doi.org/10.1016/j.ensm.2023.01.021.
[9] W. Zhang, W. Huang, Q. Zhang, Organic materials as electrodes in potassium-ion batteries, Chem–Eur J. 27 (20) (2021) 6131–6144, https://doi.org/10.1002/chem.202005259.
[10] K. Zhang, Z. Gu, E. Ang, J. Guo, X. Wang, Y. Wang, X. Wu, Advanced polyanionic electrode materials for potassium-ion batteries: progresses, challenges and application prospects, Mater. Today 54 (2022) 189–201, https://doi.org/10.1016/j.mattod.2022.02.013.
[11] H. Sun, H. Ryu, U. Kim, J.A. Weeks, A. Heller, Y. Sun, C.B. Mullins, Beyond doping and coating: prospective strategies for stable high-capacity layered Ni-rich cathodes, ACS Energy Lett. 5 (4) (2020) 1136–1146, https://doi.org/10.1021/acsenergylett.0c00191.
[12] A. Eftekhari, Potassium secondary cell based on prussian blue cathode, J. Power Sources 126 (1–2) (2004) 221–228, https://doi.org/10.1016/j.jpowsour.2003.08.007.
[13] Z. Xiao, X. Wang, J. Meng, H. Wang, Y. Zhao, L. Mai, Advances and perspectives on one-dimensional nanostructure electrode materials for potassium-ion batteries, Mater. Today 56 (2022) 114–134, https://doi.org/10.1016/j.mattod.2022.05.009.
[14] S. Kumakura, Y. Tahara, S. Sato, K. Kubota, S. Komaba, P′2-$Na_{2/3}Mn_{0.9}Me_{0.1}O_2$ (Me = Mg, Ti, Co, Ni, Cu, and Zn): correlation between orthorhombic distortion and electrochemical property, Chem. Mater 29 (21) (2017) 8958–8962, https://doi.org/10.1021/acs.chemmater.7b02772.
[15] Y. Liu, C. Wang, S. Zhao, L. Zhang, K. Zhang, F. Li, J. Chen, Mitigation of Jahn–Teller distortion and Na^+/vacancy ordering in a distorted manganese oxide cathode material by Li substitution, Chem. Sci. 12 (2021) 1062–1067, https://doi.org/10.1039/D0SC05427E.
[16] J. Zhang, J. Kim, J. Zhang, G. Lee, M. Chen, V.W. Lau, K. Zhang, S. Lee, C. Chen, T. Jeon, Y. Kwon, Y. Kang, Regulating Pseudo-Jahn–Teller effect and superstructure in layered cathode materials for reversible alkali-ion intercalation, J. Am. Chem. Soc 144 (17) (2022) 7929–7938, https://doi.org/10.1021/jacs.2c02875.
[17] B. Peng, Y. Chen, F. Wang, Z. Sun, L. Zhao, X. Zhang, W. Wang, G. Zhang, Unusual Site-selective doping in layered cathode strengthens electrostatic cohesion of alkali-metal layer for practicable sodium-ion full cell, Adv. Mater. 34 (2022) 2103210, https://doi.org/10.1002/adma.202103210.
[18] Q. Zhang, D. Christophe, W.K. Pang, Y. Liu, Z. Wang, V.K. Peterson, J. Mao, Z. Guo, Structural insight into layer gliding and lattice distortion in layered manganese oxide electrodes for potassium-ion batteries, Adv. Energy Mater. 9 (30) (2019) 1900568, https://doi.org/10.1002/aenm.201900568.
[19] B. Zhang, Y. Zhang, X. Wang, H. Liu, Y. Yan, S. Zhou, Y. Tang, G. Zeng, X. Wu, H. G. Liao, Y. Qiu, H. Huang, L. Zheng, J. Xu, W. Yin, Z. Huang, Y. Xiao, Q. Xie, D. L. Peng, C. Li, Y. Qiao, S.G. Sun, Role of substitution elements in enhancing the structural stability of Li-rich layered cathodes, J. Am. Chem. Soc 145 (15) (2023) 8700–8713, https://doi.org/10.1021/jacs.3c01999.
[20] T. Wu, X. Liu, X. Zhang, Y. Lu, B. Wang, Q. Deng, Y. Yang, E. Wang, Z. Lyu, Y. Li, Y. Wang, Y. Lyu, C. He, Y. Ren, G. Xu, X. Sun, K. Amine, H. Yu, Full concentration gradient-tailored Li-rich layered oxides for high-energy lithium-ion batteries, Adv. Mater. 33 (2) (2021) 2001358, https://doi.org/10.1002/adma.202001358.
[21] D. Darbar, N. Muralidharan, R.P. Hermann, J. Nanda, I. Bhattacharya, Evaluation of electrochemical performance and redox activity of Fe in Ti doped layered P2-$Na_{0.67}Mn_{0.5}Fe_{0.5}O_2$ cathode for sodium ion batteries, Electrochim. Acta 380 (1) (2021) 138156, https://doi.org/10.1016/j.electacta.2021.138156.
[22] R. Luo, X. Li, J. Ding, J. Bao, C. Ma, C. Du, X. Cai, X. Wu, Y. Zhou, Suppressing Jahn-Teller distortion and phase transition of $K_{0.5}MnO_2$ by K-site Mg substitution for potassium-ion batteries, Energy Storage Mater. 47 (2022) 408–414, https://doi.org/10.1016/j.ensm.2022.02.027.
[23] Z. Xiao, F. Xia, L. Xu, X. Wang, J. Meng, H. Wang, X. Zhang, L. Geng, J. Wu, L. Mai, Suppressing the Jahn–Teller effect in Mn-based layered oxide cathode toward long-life potassium-ion batteries, Adv. Funct. Mater. 32 (14) (2022) 2108244, https://doi.org/10.1002/adfm.202108244.
[24] X. Li, X. Ma, D. Su, L. Liu, R. Chisnell, S.P. Ong, H. Chen, A. Toumar, J. Idrobo, Y. Lei, J. Bai, F. Wang, J.W. Lynn, Y.S. Lee, G. Ceder, Direct visualization of the Jahn–Teller effect coupled to Na ordering in $Na_{5/8}MnO_2$, Nat. Mater. 13 (6) (2014) 586–592, https://doi.org/10.1038/nmat3964.
[25] N. Manson, Z. Hasan, C. Flint, Jahn-Teller effect in the $^4T_{2g}$ state of Mn^{4+} in Cs_2SiF_6, J. Phys. C: Solid State Phys. 12 (1979) 5483–5488, https://doi.org/10.1088/0022-3719/12/24/020.
[26] H. Hu, Y. Zhu, Y. Xiao, S. Li, J. Li, Z. Hao, J. Zhao, S. Chou, Strain engineering by local chemistry manipulation of triphase heterostructured oxide cathodes to facilitate phase transitions for high-performance sodium-ion batteries, Adv. Energy Mater. 12 (32) (2022) 2201511, https://doi.org/10.1002/aenm.202201511.
[27] M.C.M. O'Brien, Dynamic Jahn-Teller effect in an orbital triplet state coupled to both E_g and T_{2g} vibrations, Phys. Rev. 187 (2) (1969) 407, https://doi.org/10.1103/PhysRev.187.407.
[28] P. Yan, J. Zheng, M. Gu, J. Xiao, J. Zhang, C. Wang, Intragranular cracking as a critical barrier for high-voltage usage of layer-structured cathode for lithium-ion batteries, Nat. Commun. 8 (2017) 14101, https://doi.org/10.1038/ncomms14101.
[29] P. Yan, J. Zheng, T. Chen, L. Luo, Y. Jiang, K. Wang, M. Sui, J. Zhang, S. Zhang, C. Wang, Coupling of electrochemically triggered thermal and mechanical effects to aggravate failure in a layered cathode, Nat. Commun. 9 (2018) 2437, https://doi.org/10.1038/s41467-018-04862-w.
[30] S.C. Tarantino, M. Giannini, M.A. Carpenter, M. Zema, Cooperative Jahn–Teller effect and the role of strain in the Ttragonal-to-cubic phase transition in $Mg_xCu_{1-x}Cr_2O_4$, IUCr 3 (2016) 354–366, https://doi.org/10.1107/S2052252516012574.
[31] I.B. Bersuker, Jahn–Teller and Pseudo-Jahn–Teller effects: from particular features to general tools in exploring molecular and solid state properties, Chem. Rev. 121 (3) (2020) 1463–1512, https://doi.org/10.1021/acs.chemrev.0c00718.
[32] S. Zhao, Z. Liu, G. Xie, Z. Guo, S. Wang, J. Zhou, X. Xie, B. Sun, S. Guo, G. Wang, High-efficiency cathode potassium compensation and interfacial stability improvement enabled by dipotassium squarate for potassium-ion batteries, Energy Environ. Sci. 12 (2022) 3015–3023, https://doi.org/10.1039/D2EE00833E.
[33] H. Wang, H. Peng, Z. Xiao, R. Yu, F. Liu, Z. Zhu, L. Zhou, J. Wu, Double-layer phosphates coated Mn-based oxide cathodes for highly stable potassium-ion batteries, Energy Storage Mater. 58 (2023) 101–109, https://doi.org/10.1016/j.ensm.2023.03.016.
[34] B. Wang, E. Ang, Y. Yang, Y. Zhang, M. Ye, Q. Liu, C. Li, Post-lithium-ion battery era: recent advances in rechargeable potassium-ion batteries, Chem. Eur. J. 27 (2021) 512–536, https://doi.org/10.1002/chem.202001811.